

# Flow mediated interactions between two cylinders at finite Re numbers

Mattia Gazzola,<sup>1</sup> Chloe Mimeau,<sup>2</sup> Andrew A. Tchieu,<sup>1</sup>  
and Petros Koumoutsakos<sup>1,a)</sup>

<sup>1</sup>*Institute of Computational Science, ETH Zurich, CH-8032 Zurich, Switzerland*

<sup>2</sup>*Institut de Mathématiques de Bordeaux, Université Bordeaux 1, Talence 33400, France*

(Received 21 December 2011; accepted 29 March 2012; published online 23 April 2012)

We present simulations of two interacting moving cylinders immersed in a two-dimensional incompressible, viscous flow. Simulations are performed by coupling a wavelet-adapted, remeshed vortex method with the Brinkman penalization and projection approach. This method is validated on benchmark problems and applied to simulations of a master-slave pair of cylinders. The master cylinder's motion is imposed and the slave cylinder is let free to respond to the flow. We study the relative role of viscous and inertia effects in the cylinders interactions and identify related sharp transitions in the response of the slave. The observed differences in the behavior of cylinders with respect to corresponding potential flow simulations are discussed. In addition, it is observed that in certain situations the finite size of the slave cylinders enhances the transport so that the cylinders are advected more effectively than passive tracers placed, respectively, at the same starting position. © 2012 American Institute of Physics. [<http://dx.doi.org/10.1063/1.4704195>]

## I. INTRODUCTION

Flows generated by neighboring, moving objects affect their mutual behavior, leading to complex collective phenomena emerging from flow-structure interactions. Flow mediated interactions are intrinsic to natural phenomena such as fish schooling,<sup>1,2</sup> dolphin drafting,<sup>3</sup> collective transport of suspensions of swimming micro-organisms,<sup>4–6</sup> sedimentation of cloud particles,<sup>7,8</sup> cluster formation,<sup>9</sup> collision avoidance,<sup>10</sup> and egg fertilization.<sup>11</sup>

The flow physics of these complex interactions has been the subject of experimental and computational investigations that aim to unveil governing mechanisms,<sup>1–6</sup> and may be in turn exploited for engineering applications ranging from collaborating underwater devices to swarms of unmanned air vehicles and energy harvesting devices.<sup>12,13</sup>

Fluid mediated interactions between moving objects have been investigated in the inertia-less limit ( $Re = 0$ ) via Stokesian dynamics,<sup>4,5,14–16</sup> and for small, but finite, Reynolds number ( $Re \ll 1$ ) through Oseen equations.<sup>17</sup> Hydrodynamic interactions in inviscid fluids ( $Re = \infty$ ) have been modeled by potential flow theory for bodies in the presence of free surfaces or bodies immersed in fluids.<sup>18,19</sup> There has been relatively little effort in characterizing hydrodynamic coupling on the motion of immersed objects for finite, moderate Reynolds numbers ( $1 \leq Re \leq 10^4$ ).<sup>10,20,21</sup> We note also the work of Eldredge in developing a formulation that aims to bridge viscous and inviscid descriptions.<sup>22</sup> Viscous flow simulations imply the generation of vorticity on the surfaces of the bodies and their interactions are in turn mediated by the transport and dissipation of these vortices.

Varying the ratio between viscous and inertial effects could drastically affect the qualitative response of the system. For example, the onset of schooling seems to coincide with a transition from viscous to inertial environments ( $Re \sim 1000$ ).<sup>23,24</sup> Other examples include the behavior of clusters of particles in a vibrating fluid, where a wide variety of patterns seem to be achievable by varying

a)Electronic mail: [petros@inf.ethz.ch](mailto:petros@inf.ethz.ch).

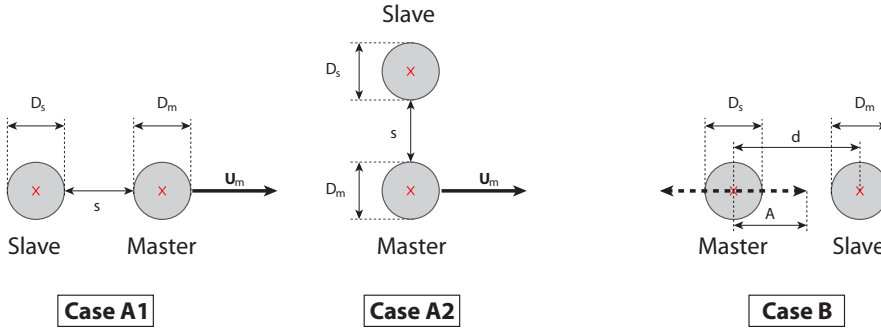


FIG. 1. Case A1: The set up consists of a master of diameter  $D_m$ , forced to move forward at the constant velocity  $\mathbf{U}_m$ , and a slave of diameter  $D_s$ , initially located behind the master at the separation distance  $s$ . Case A2: The set up consists of a master of diameter  $D_m$ , forced to move forward at the constant velocity  $\mathbf{U}_m$ , and a slave of diameter  $D_s$ , initially located above the master at the separation distance  $s$ . Case B: The set up consists of a master of diameter  $D_m$  and a slave of diameter  $D_s$ , initially located beside the master at a distance  $d$  between the centers of mass. The master is forced to oscillate horizontally according to  $\mathbf{x}_m = A \sin(2\pi t/\mathcal{T} + \phi)$ ,  $\mathbf{x}_m$  being the master's location of its center of mass and  $A$ ,  $\mathcal{T}$ , and  $\phi$ , respectively, the oscillation amplitude, period, and phase.

the  $Re$  between 2 and 10,<sup>9</sup> or the change in behavior of a gravity-driven dense suspension jet around  $Re \sim 1$ .<sup>8</sup>

In this study, we assess the role of viscous interactions by performing simulations of a prototypical system of interacting bodies consisting of two moving cylinders immersed in a two-dimensional viscous, incompressible flow. In these simulations the motion of one cylinder (master) is imposed, while the other (slave) is free to respond to the flow. The interaction between master and slave is purely flow mediated, as no contact is taken into account. Inspired by the works of Nair and Kanso<sup>18</sup> and Tchieu *et al.*<sup>19</sup> we consider three configurations as illustrated in Figure 1. In cases A1 and A2 (cases described below), the master cylinder moves forward at a constant velocity, while in case B it is forced to oscillate horizontally. We investigate the slave's response and we compare our findings with those of inviscid simulations<sup>19</sup> in order to assess the role of viscous effects, vorticity generation, and transport on these interactions.

In the present paper, the Navier-Stokes equations are solved using a multiresolution, remeshed vortex method<sup>25–27</sup> while the enforcement of the no-slip boundary conditions and the interaction of the objects with the surrounding fluid is realized through a Brinkman penalization technique.<sup>21,28,29</sup> The feedback from the fluid to the freely moving cylinder is captured through the projection method which, by letting the fluid evolve inside the objects, allows one to compute the transfer of linear and angular momenta to the body.<sup>21,29</sup> The remeshed vortex methods are coupled with wavelet based adaptivity to increase computational efficiency.<sup>27,30–32</sup>

The paper is organized as follows. In Sec. II the numerical method is described while its validation and convergence properties are illustrated in Sec. III. Its application to several fluid mediated problems is presented in Sec. IV. The findings of this work are summarized in Sec. V.

## II. GOVERNING EQUATIONS AND NUMERICAL METHOD

We consider a two-dimensional incompressible, viscous flow in an infinite domain ( $\Sigma$ ), in which a collection of  $N$  moving rigid bodies are immersed. We denote with  $\Omega_i$ ,  $i = 1, \dots, N$  the support of the solids, which are assumed to be of the same density of the fluid ( $\rho = 1$ ). The flow field is described by the Navier-Stokes equations (Eqs. (1) and (2)) along with the no-slip boundary conditions at the surface of the bodies  $\partial\Omega_i$  (Eq. (3)), while the feedback from the fluid to the freely moving bodies is governed by Newton's equation of motion (Eqs. (4) and (5)):

$$\frac{\partial \mathbf{u}}{\partial t} + (\mathbf{u} \cdot \nabla) \mathbf{u} = -\frac{1}{\rho} \nabla p + \nu \nabla^2 \mathbf{u}, \quad \mathbf{x} \in \Sigma \setminus \Omega_i, \quad (1)$$

$$\nabla \cdot \mathbf{u} = 0, \quad \mathbf{x} \in \Sigma \setminus \Omega_i, \quad (2)$$

$$\mathbf{u} = \mathbf{u}_i, \quad \mathbf{x} \in \partial\Omega_i, \quad (3)$$

$$m_i \ddot{\mathbf{x}}_i = \mathbf{F}_i^H, \quad (4)$$

$$\frac{d(I_i \dot{\theta}_i)}{dt} = \mathbf{M}_i^H, \quad (5)$$

where  $\nu$  is the kinematic viscosity,  $\mathbf{u}_i$ ,  $\mathbf{x}_i$ ,  $m_i$ ,  $I_i$  and  $\theta_i$  are, respectively, the velocity, the position of the center of mass, the mass, the moment of inertia, and the angular velocity of the body  $i$ , while  $\mathbf{F}_i^H$  and  $\mathbf{M}_i^H$  are the hydrodynamic force and momentum exerted by the fluid on the body  $i$ .

This system of equations (Eqs. (1)–(5)) is solved by combining remeshed vortex methods<sup>25,26,33,34</sup> and Brinkman penalization<sup>28,35–37</sup> with a projection approach<sup>21,29,38</sup> and interface tracking via level sets. Adding the penalization term and rewriting the momentum equation in its velocity-vorticity ( $\mathbf{u}-\omega$ , where  $\omega = \nabla \times \mathbf{u}$ ) formulation, Eqs. (1) and (2) become

$$\frac{\partial \omega}{\partial t} + \nabla \cdot (\mathbf{u}\omega) = \nu \nabla^2 \omega + \sum_{i=1}^N \lambda \nabla \times \chi_i (\mathbf{u}_i - \mathbf{u}), \quad \mathbf{x} \in \Sigma, \quad (6)$$

$$\nabla \cdot \mathbf{u} = 0, \quad \mathbf{x} \in \Sigma, \quad (7)$$

where  $\chi_i$  are the characteristic functions describing the bodies (one inside, zero outside) and  $\lambda \gg 1$  is the penalization factor. The velocity field  $\mathbf{u}$  is computed from vorticity by solving the unbounded Poisson equation,  $\nabla^2 \mathbf{u} = -\nabla \times \omega$ . Translational ( $\mathbf{u}_i^t$ ) and rotational ( $\mathbf{u}_i^r$ ) components of  $\mathbf{u}_i = \mathbf{u}_i^t + \mathbf{u}_i^r$  are recovered through a projection approach.<sup>21,29</sup> The combined use of such techniques bypasses the direct estimation of hydrodynamic forces and momenta acting on the immersed bodies and has been proven to capture accurately the fluid-structure interactions between multiple solids and the flow.<sup>21</sup>

Remeshed vortex methods rely on the regularization of the vortex particles on an underlying cartesian grid and interpolation of the vorticity carried by the particles through a high order kernel such as the  $M'_4$ .<sup>25,26,33,34</sup> The presence of an underlying regular grid also allows for the fast evaluation of all differential operators using finite difference schemes. Furthermore, the regularized grid enables the use of wavelet based adaptivity.<sup>30,31</sup> The grid nodes are adapted according to a wavelet multiresolution analysis of the vorticity and velocity fields in order to capture the emergence (grid refinement) or disappearance (grid compression) of small scales. Refinement, computing, and compression stages regularly alternate while evolving the solution of the system in time.

The solution of the Poisson equation on multiresolution regular grids is obtained through a fast multiple method (FMM) thus accommodating the far field boundary condition.<sup>39,40</sup> The description of the use of FMM with wavelet based adaptivity for incompressible flows past bluff bodies is given by Rossinelli.<sup>41</sup>

$$\text{refinement: } \mathcal{R}(\omega^n \text{ and } \mathbf{u}^n)|_{t_r}, \quad (8)$$

$$\nabla^2 \psi^n = -\omega^n, \quad (9)$$

$$\mathbf{u}^n = \nabla \times \psi^n, \quad (10)$$

$$\mathbf{u}_i^{t,n} = \frac{1}{m_i} \int_{\Sigma} \rho \chi_i^n \mathbf{u}^n d\mathbf{x}, \quad (11)$$

$$\dot{\theta}_i^n = \frac{1}{I_i} \int_{\Sigma} \rho \chi_i^n (\mathbf{x} - \mathbf{x}_i^n) \times \mathbf{u}^n d\mathbf{x}, \quad (12)$$

$$\mathbf{u}_i^{r,n} = \dot{\theta}_i^n \times (\mathbf{x} - \mathbf{x}_i^n), \quad (13)$$

$$\mathbf{u}_{\lambda}^n = \frac{\mathbf{u}^n + \lambda \Delta t \sum_{i=1}^N \chi_i^n (\mathbf{u}_i^{t,n} + \mathbf{u}_i^{r,n})}{1 + \lambda \Delta t \sum_{i=1}^N \chi_i^n}, \quad (14)$$

$$\omega_\lambda^n = \nabla \times \mathbf{u}_\lambda^n, \quad (15)$$

$$\frac{\partial \omega_\lambda^n}{\partial t} = \nu \nabla^2 \omega_\lambda^n, \quad (16)$$

$$\frac{\partial \omega_\lambda^n}{\partial t} + \nabla \cdot (\mathbf{u}_\lambda^n \omega_\lambda^n) = 0, \quad (17)$$

$$\omega^{n+1} = \omega_\lambda^{n+1}, \quad (18)$$

$$\mathbf{x}_i^{n+1} = \mathbf{x}_i^n + \mathbf{u}_i^{t,n} \Delta t^n, \quad (19)$$

$$\theta_i^{n+1} = \theta_i^n + \dot{\theta}_i^n \Delta t^n, \quad (20)$$

$$\text{compression: } \mathcal{C}(\omega^{n+1} \text{ and } \mathbf{u}^{n+1})|_{t_c}. \quad (21)$$

A time-step from  $t^n$  to  $t^{n+1}$  is detailed by Eqs. (8)–(21), assuming that all quantities are known up to time  $t^n$ . We denote with  $\mathcal{R}(a)|_{t_r}$  and with  $\mathcal{C}(a)|_{t_c}$ , respectively, the refinement and compression stages given the wavelet analysis of the field  $a$ , using the refinement and compression thresholds  $t_r$  and  $t_c$ . Throughout this work, if not specified otherwise, we consider the domain  $\Sigma = [0, 1] \times [0, 1]$ , set  $\lambda = 10^4$ ,  $t_r = 10^{-4}$ ,  $t_c = 10^{-6}$ , Lagrangian CFL condition<sup>42</sup>  $LCFL = 0.1$ , and implement  $\chi$  to follow the definition of Gazzola *et al.*,<sup>21</sup> with smoothing length  $\epsilon = \sqrt{2}h^e$ , where  $h^e$  is the minimum allowed grid spacing in the multiresolution representation. Hereafter, we will refer to  $h^e$  as effective grid spacing and to  $ER = 1/h^e$  as the effective resolution. All spatial operators are discretized with fourth-order accurate schemes, except for the fifth-order average interpolating wavelets. Time integration is carried out via Gudonov splitting: the penalization term (Eqs. (14) and (15)) is treated with an implicit Euler scheme, diffusion (Eq. (16)) through a second-order Runge-Kutta scheme coupled with local time stepping,<sup>30,41</sup> particle advection (Eq. (17)) via a second-order Runge-Kutta scheme and body advection (Eqs. (19) and (20)) with a first-order explicit Euler scheme. The present algorithm is implemented using the multi-resolution adapted grids (MRAG) library.<sup>30,31,41</sup>

### III. VALIDATION

We present a validation study of the computational methods employed in this work (Sec. II). We consider the flow past an impulsively started cylinder to validate the remeshed vortex method along with the penalization approach. In addition, we consider the problem of two cylinders in the course of a collision and compute the forces induced by the fluid on the two cylinders to validate the numerical scheme for fluid mediated interactions. The space and time convergence properties of the numerical scheme (Sec. II) are investigated by performing simulations for the test case B.

#### A. Flow past impulsively started cylinder at $Re = 1000$

Flow past an impulsively started cylinder is a challenging problem for computational methods due to the singularity of the forces acting on the body at early times and the cascade of vortical structures emerging over time. In the domain  $\Sigma = [0, 1] \times [0, 1]$ , we considered a cylinder of diameter  $D = 0.05$ , initially located at  $(0.4, 0.5)$ , moving at constant velocity  $\mathbf{U}_T = 0.1$  (i.e.,  $\mathbf{u}^t = \mathbf{U}_T$ ,  $\mathbf{u}^r = 0$ ), impulsively started in an incompressible, viscous flow at  $Re = |\mathbf{U}_T|D/\nu = 1000$ . Furthermore, we set  $ER = 8192 \times 8192$ ,  $LCFL = 0.01$  and  $\epsilon = 2\sqrt{2}h^e$ . As can be seen in Fig. 2, the drag coefficient  $C_d = 2F_x/(|\mathbf{U}_T|D)$  computed here by integrating the penalization term  $\mathbf{F} = -\int_{\Sigma} \chi(\mathbf{U}_T - \mathbf{u})d\mathbf{x}$ , compares well with reference simulations and its evolution in time is accurately captured, with a discrepancy found to be less than 1% at all times.<sup>25</sup>

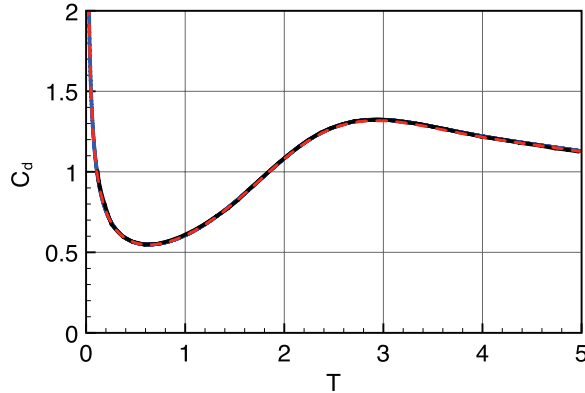


FIG. 2. Drag coefficient ( $C_d$ ) evolution against dimensionless time  $T = 2|U_T|t/D$  for flow past impulsively started cylinder at  $Re = 1000$ . The dotted (red) line was obtained setting  $ER = 8192 \times 8192$ ,  $LCFL = 0.01$ , and  $\epsilon = 2\sqrt{2}h^e$ . Solid (black and blue) lines are, respectively, reference solutions of Refs. 25 and 37. Since the discrepancy is negligible, the three solutions overlap and the two solid lines are nearly indistinguishable.

### B. Inline impact of two cylinders without a free stream

We considered as a reference the system investigated by Bampalias and Graham.<sup>10</sup> The system involves two cylinders, in a viscous, incompressible flow, impulsively started and approaching each other by moving at the same constant velocity along the line connecting their centers. At impact, their motion is instantaneously stopped and the two cylinders remain stationary. In Bampalias and Graham simulations were performed using a Galerkin weighted residual finite element method with a body fitted mesh and the authors report flow induced force coefficients ( $C_d$ ) acting on either cylinder as function of the Reynolds number.

In Fig. 3(a), we report the comparison between the forces presented in Bampalias and Graham<sup>10</sup> and the forces computed by the present methodology for  $Re = 25, 50, 100$ , and  $200$ . We note that the forces computed by the integration of the penalization term, as in Sec. III A, are readily extended to multiple bodies. Our results are in good agreement with the results of the reference simulations before impact, even though for  $Re = 100$  and  $Re = 200$ , discrepancies tend to appear when approaching collision. After impact, for all  $Re$  investigated, discrepancies are found to be larger during the transient post collision. As pointed out in Bampalias and Graham,<sup>10</sup> the distortion of the numerical elements, and subsequent remeshing, especially approaching contact, maybe be source of oscillations and loss of accuracy in their approach. This observation may explain why their method does not effectively capture the singularity event (evident for  $Re = 100$ ) and thus the differences with our solution after impact.

Our simulations were carried out in a computational domain  $\Sigma = [0, 1] \times [0, 1]$ , initializing two cylinders of diameter  $D = 0.05$  at a distance between their centers of  $L = 3D$  and moving towards each other with a velocity  $\mathbf{U}$  set to one diameter  $D$  per time unit. Force coefficients  $C_d$  were reported in Fig. 3 against the dimensionless time  $T^* = |\mathbf{U}|(t - t_{impact})/D$ . Furthermore, we set  $ER = 8192 \times 8192$ ,  $LCFL = 0.1$  and  $\epsilon = \sqrt{2}h^e$ .

### C. In-line impact of two cylinders in uniform free stream

In this section, we considered the impact between two inline cylinders immersed in a uniform free stream ( $\mathbf{U}_\infty$ ), as detailed by Bampalias and Graham.<sup>10</sup> The upstream cylinder is stationary, while the downstream cylinder moves towards the first one at a constant velocity  $\mathbf{U} = -\mathbf{U}_\infty$ . After collision both cylinders remain stationary. In this case, the flow induced forces acting on the bodies are no longer symmetric due to the interaction of the upstream cylinder's wake with the second cylinder.

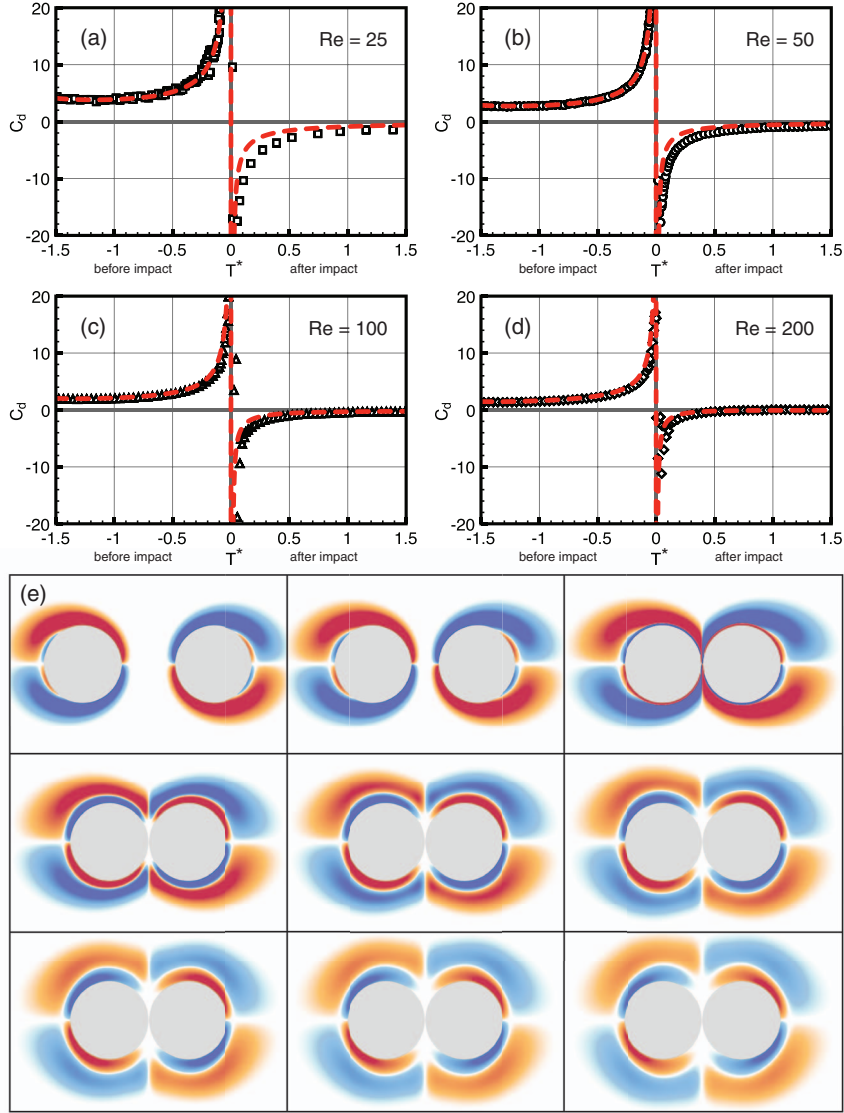


FIG. 3. Inline impact of two cylinders without free stream. (a)–(d) Evolution of the force coefficient  $C_d$  against the dimensionless time  $T^*$  for, respectively,  $Re = 25, 50, 100$ , and  $200$ . Dotted (red) lines and symbols represent, respectively, the solutions of the present method and Bampalas and Graham.<sup>10</sup> (e) Given from left to right and top to bottom is the time sequence of the vorticity field ( $-0.66 \leq T^* \leq 2$ ,  $\Delta T^* = 0.33$ ).

We report a comparison of the measured force coefficients ( $C_d$ ) at  $Re = 100$  in Fig. 4(a). For completeness we also report the evolution of net force coefficients after collision in Fig. 4(b), and corresponding vorticity fields in Fig. 4(c). We note that force coefficients acting on the upstream and downstream cylinders agree well with the reference solution.<sup>10</sup>

Simulations were performed in a computational domain  $\Sigma = [0, 1] \times [0, 1]$ , setting the free stream velocity  $\mathbf{U}_\infty$  to one diameter  $D$  per physical time unit and initializing the two cylinders of diameter  $D = 0.0125$  at a distance of  $L = 15D$  between their centers. In Bampalas and Graham,<sup>10</sup> the two cylinders were initialized closer to each other and their wakes were let to develop for an unspecified time, before impulsively starting the downstream cylinder. Here we opted for a starting condition in which the downstream cylinder is impulsively started while initially located far enough to ensure the development of the upstream wake. Force coefficients  $C_d$  are reported in Fig. 4 against

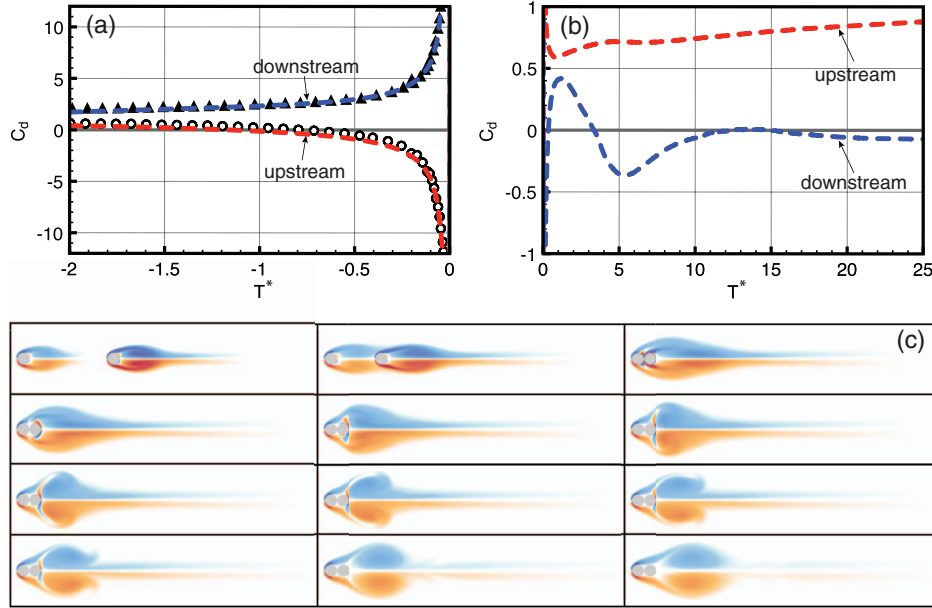


FIG. 4. Inline impact of two cylinders in uniform free stream. (a) and (b) Evolution of the force coefficient  $C_d$  against the dimensionless time  $T^*$  at  $Re = 100$  before (a) and after (b) collision. Circles and triangles correspond, respectively, to upstream and downstream cylinders according to Bampalis and Graham.<sup>10</sup> Dashed lines (red and blue) correspond, respectively, to upstream and downstream cylinders in the present computations. (c) From left to right and top to bottom, vorticity fields at times  $T^* = -13.3, -6.7, 0, 1.7, 3.3, 5, 6.7, 8.3, 10, 11.7, 18.3, 25$ .

the dimensionless time  $T^* = |\mathbf{U}|(t - t_{impact})/D$ . Furthermore, we set the effective resolution of the multiresolution solver to  $ER = 16\,384 \times 16\,384$  with  $LCFL = 0.1$  and  $\epsilon = \sqrt{2}h^e$ .

#### D. Convergence study

We performed a convergence study in space and time, for the test case B (Fig. 1). In the computational domain  $\Sigma = [0, 1] \times [0, 1]$ , we considered two equally sized cylinders ( $D_m = D_s = 0.05$ ), initially located at  $(0.4, 0.5)$  and  $(0.525, 0.5)$  and the Reynolds number  $Re = |\mathbf{U}_m|D_m/\nu = 100$  (for further simulation details see Fig. 5 and Sec. IV B). Convergence orders were determined by computing the  $L^1$ ,  $L^2$ , and  $L^\infty$  norm of the error  $e(t) = \|\mathbf{x}_{cm\ best\ resolved}(t) - \mathbf{x}_{cm}(t)\|$ , where  $\mathbf{x}_{cm}$  is the slave's center of mass location.

Regarding space convergence, two different studies were performed by varying the effective resolution  $ER$  between  $512 \times 512$  and  $4096 \times 4096$  with  $16\,384 \times 16\,384$  as best resolved case, and setting  $LCFL = 0.01$ . In the first study, we fixed the model by setting the mollification length proportional to the coarsest effective grid spacing ( $\epsilon = \sqrt{2}h_{512}^e$ ). In the second study, the ratio  $\epsilon/h^e$  is chosen to be constant to investigate the convergence to the actual geometry. As we can see in Fig. 5, the method shows third order convergence ( $L^1 = 3, L^2 = 3, L^\infty = 3$ ) fixing  $\epsilon = \sqrt{2}h_{512}^e$  and between first and second order ( $L^1 = 1.4, L^2 = 1.5, L^\infty = 1.5$ ) fixing  $\epsilon/h^e = \sqrt{2}$ . Given the second order smoothing function used in Ref. 21 for  $\chi$ , we expect, for the fixed model case, a space convergence order lower than 4 but greater than 2, due to the compact limited support of the mollified region.

Time convergence study was performed setting  $ER = 4096 \times 4096$  and  $\epsilon = \sqrt{2}h^e$  and varying  $LCFL$  between 0.1 and 0.003 with 0.001 as best resolved case. The order of convergence was found to be between first and second ( $L^1 = 1.2, L^2 = 1.74, L^\infty = 1.2$ ) (Fig. 5(c)). Time integration is performed via Godunov splitting, entailing a mix of first and second order operators (second order Runge-Kutta for Eqs. (16) and (17), implicit Euler for Eq. (14) and first order explicit Euler for Eqs. (19) and (20)), thus we expect a convergence rate between one and two. We conclude that the

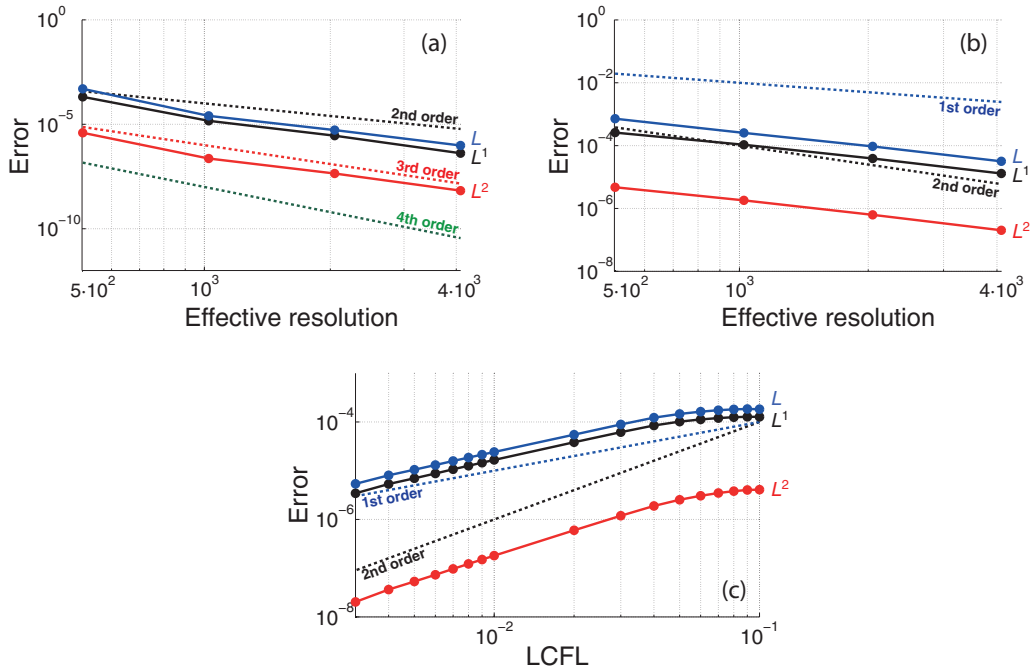


FIG. 5. Convergence study for case B. The master oscillates horizontally according to Fig. 1. The amplitude was set to  $A = D_m$ , period  $T = 1$  physical time unit,  $\phi = 0$ , and simulations were carried out up to physical time  $t = 1.5T$ . (a) Space convergence (mollification length fixed based on  $ER$ ,  $\epsilon = \sqrt{2}h_{S12}^e$ ):  $L^\infty(e)$  (blue),  $L^1(e)$  (black), and  $L^2(e)$  (red) are plotted against  $ER$ .  $LCFL$  was set to 0.01. (b) Space convergence (ratio  $\epsilon/h^e$  fixed to  $\sqrt{2}$ ):  $L^\infty(e)$  (blue),  $L^1(e)$  (black), and  $L^2(e)$  (red) are plotted against  $ER$ .  $LCFL$  was set to 0.01. (c) Time convergence:  $L^\infty(e)$  (blue),  $L^1(e)$  (black), and  $L^2(e)$  (red) are plotted against  $LCFL$ .  $ER$  was set to  $4096 \times 4096$ . For all studies we used  $\lambda = 10^4$ . Dashed lines (blue, black, red, green) represent (respectively) first, second, third, and fourth order slopes.

convergence rates of the method are in agreement with the spatial and time discretization of the differential operators.

## IV. RESULTS

### A. Slave's response to master's forward motion: Case A

In this section, inspired by the work of Tchieu *et al.*,<sup>19</sup> we consider the slave's response to a master's imposed forward motion (Fig. 1, cases A1 and A2). We performed simulations of incompressible, viscous flow in which the master is impulsively started and the slave is *initially at rest*. The Reynolds number and the slave's diameter are varied in order to assess their influence on the system's behavior. It is noted that cases A1 and A2 do not have the same initial conditions as Tchieu *et al.*,<sup>19</sup> where the slave is initially moving with the master cylinder then passively advected by the fluid mediated interactions for  $t > 0$ . In a viscous simulation, if the slave is given an impulsive velocity at time  $t = 0$ , the drag on the cylinder at  $t = 0^+$  is infinite due to finite Reynolds number effects, therefore we have chosen to study the analogous problem where the slave cylinder is initially at rest and then subsequently moves solely under the influence of the master cylinder for  $t > 0$ .

Simulations were carried out in the computational domain  $\Sigma = [0, 1] \times [0, 1]$ , where the master of diameter  $D_m = 0.025$ , initialized at  $(0.2, 0.5)$ , travels at the constant velocity of  $2D_m$  per physical time unit. For both cases, A1 and A2, we considered three different slave's diameters, namely,  $D_s = D_m$ ,  $D_s = D_m/2$ , and  $D_s = D_m/4$ , for which we set, respectively,  $ER = 4096 \times 4096$ ,  $ER = 4096 \times 4096$ , and  $ER = 8192 \times 8192$ . Furthermore, for each subcase, the Reynolds number ( $Re = U_m D_m / v$ ) was varied between 10 and 500.

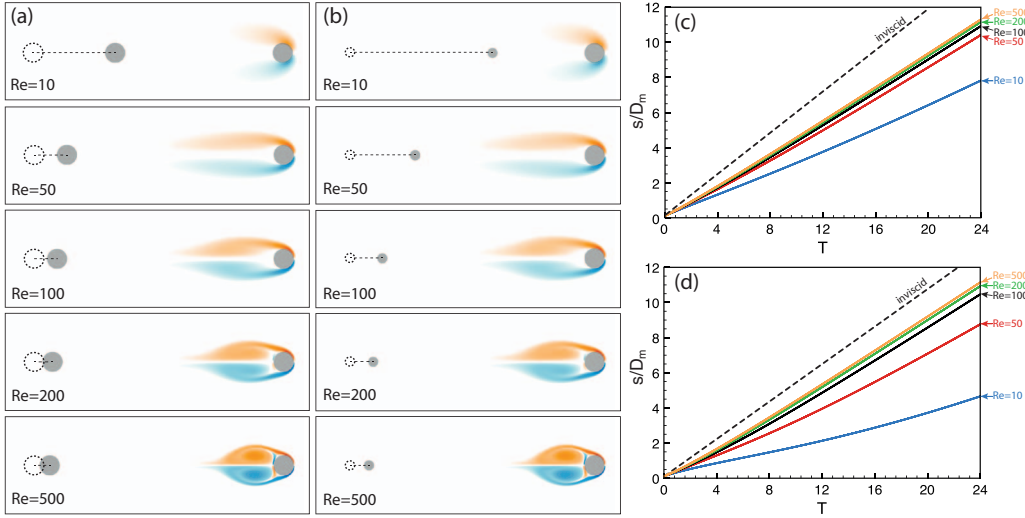


FIG. 6. Case A1. (a) Test case  $D_s = D_m$  at dimensionless time  $T = 24$ : for several  $Re$ , master and slave (full grey aft cylinder, where the initial position is represented by the dashed cylinder) are superimposed to the corresponding vorticity field. (b) Test case  $D_s = D_m/2$  at dimensionless time  $T = 24$ : vorticity fields. (c) Normalized separation distance  $s/D_m$  as function of dimensionless time  $T$  for test case  $D_s = D_m$ . (d) Normalized separation distance  $s/D_m$  as function of dimensionless time  $T$  for test case  $D_s = D_m/2$ . In (c) and (d) solid lines corresponds to  $Re = 10, 50, 100, 200$ , and 500 (blue, red, black, green, and orange, respectively) and the dotted lines refer to the inviscid solution.

### 1. Case A1

The set up of this study is depicted in Fig. 1. We focus on the effect of the Reynolds number on the trajectory of a slave initialized behind the master. In all cases of this section, the slave initially sits at rest at a separation distance  $s = D_m/10$  from the master.

For the test case  $D_s = D_m$ , results are illustrated in Fig. 6. We observe that for all  $Re$  investigated, the slave's qualitative behavior is found to be the same: the aft cylinder is accelerated from rest, travels a certain distance behind the master and progressively slows down until it stops. In all cases the separation distance  $s$  is observed to monotonically increase in time. Nevertheless, the distance travelled by the slave is larger for lower  $Re$ , indicating that a viscous flow improves the ability of the master to drag along the slave cylinder. In the test case  $D_s = D_m/2$ , we observed the same trend, although here transport is further enhanced, mainly due to the smaller inertia of the slave.

With the same configuration and initial conditions as described above, we conducted inviscid simulations following the method described in Tchieu *et al.*<sup>19</sup> In the inviscid case the slave cylinder initially moves opposite of the master cylinder because the initial impulse of the fluid is exactly opposite to the initial momentum of the forced body.<sup>18</sup> Therefore, as shown in Figs. 6 and 7, the cylinder separation grows more quickly than the viscous cases and even faster than if there were no fluid coupling. The creation and diffusion of vorticity in the wake of the viscous cases enhances the ability of the master cylinder to drag the slave cylinder in its direction of forced motion by creating a recirculating region behind the cylinder.

A further reduction in diameter to  $D_s = D_m/4$  reveals new dynamics for the slave. In particular the Reynolds number is found to be responsible of sharp transitions between slave's behaviors (Fig. 7). At  $Re = 10$ , as also observed in the previous studies,  $s$  monotonically increases in time. However, from  $Re = 20$  to  $Re = 82$ , we note that the slave is “trapped” by the master's vortical structures and is further accelerated. This effect reduces the separation distance  $s$ , which is no longer a monotonic function of time. Between  $Re = 30$  and  $Re = 70$ ,  $s$  nearly drops to zero by time  $T = 24$  (where  $T = 2|U_m|t/D_m$  is the dimensionless time). Master and slave thus travel altogether between  $Re = 20$  and  $Re = 82$ , which is the threshold value for which  $s$  is again observed to monotonically increase in time.

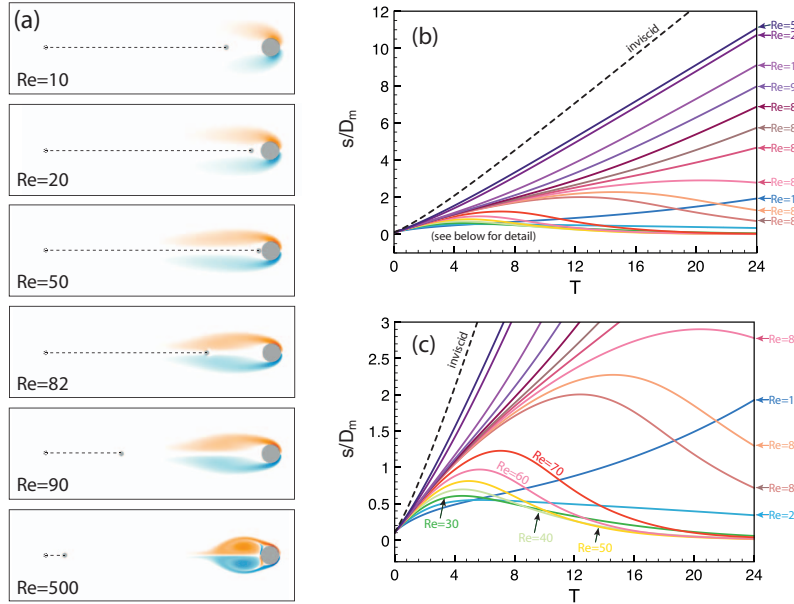


FIG. 7. Case A1. (a) Test case  $D_s = D_m/4$  at dimensionless time  $T = 24$ : for several  $Re$ , master and slave (full grey aft cylinder, where the initial position is represented by the dashed cylinder) are superimposed to the corresponding vorticity field. (b) Normalized separation distance  $s/D_m$  as function of dimensionless time  $T$ . The Reynolds number is between 10 and 500. Solid lines (of varying color) denote differing Reynolds numbers while the dotted line indicates the inviscid solution. (c) Enlargement of panel (b).

We note that we cannot exclude a similar behavior for  $D_s = D_m$  and  $D_s = D_m/2$  at  $Re < 10$ , but we could not investigate such scenarios due to the prohibitive computational costs since the time step is constrained by high viscosity. It is also noted that in all simulations the wake of the slave cylinder is negligible and thus it can be safely assumed that response of the slave cylinder is dominated by the wake produced from the master cylinder.

In order to study how the finite size of the slave cylinder's affects the interaction, we compare the slave cylinder's motion with the advection of passive tracers without the presence of the slave cylinder. We consider Reynolds numbers  $Re = 50$  and  $Re = 500$  and place the respective tracers at locations where the centers of the slave cylinders initially rest (i.e., for  $D_s/D_m = 1, 0.5, 0.25$ ,  $x/D_m = -1.1, -0.85, -0.725$  with respect to the center of the master cylinder). The tracers are advected using a second-order Runge-Kutta scheme. As depicted in Fig. 8(a), for the cases corresponding to  $D_s/D_m = 0.5, 1$ , it is seen that distance traveled  $\Delta x/D_m$  by the cylinder (dotted lines) is greater

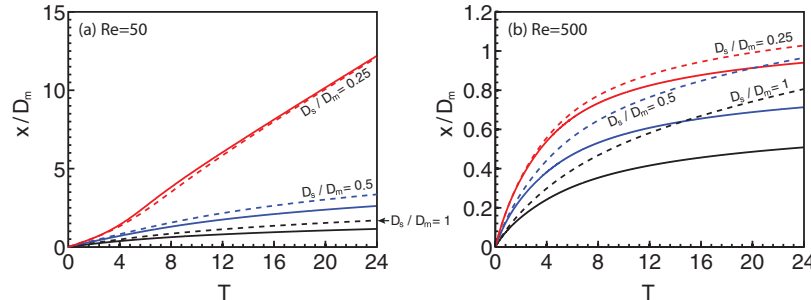


FIG. 8. The distance traveled to the right by a slave cylinder of diameter  $D_s/D_m = 0.25, 0.5, 0.25$  (dotted lines, black, blue, red, respectively) with  $s/D_m = 0.1$  and a passive tracer (solid lines) initially located at the center of the slave cylinder for (a)  $Re = 50$  and (b)  $Re = 500$ . The passive tracer is initially placed at a distance  $x/D_m = -1.1, -0.85, -0.725$  (black, blue, red) with respect to the center of the master cylinder.

than the distance traveled by the passive tracer. This suggests that the slave cylinder can be dragged further downstream than a passive tracer that is initialized at the same initial location. However, the passive tracer travels slightly further to the right when it is placed at a location corresponding to the case where the slave cylinder is  $D_s/D_m = 0.25$ . At  $Re = 500$  (Fig. 8(b)), the slave cylinder is always pulled further downstream than its passive tracer counterpart. It is also noted that in these cases, at long times, the slave cylinder drifts to the right due to its inertia whereas the passive tracers decelerate more quickly.

## 2. Case A2

In the potential flow simulations of Tchieu *et al.*,<sup>19</sup> for configurations corresponding to case A2 (see Fig. 1 for the setup), the slave was found, in some cases, to overtake the master, due to the large side forces generated by the master. Here we tested an analogous case, where the slave cylinder is initially at rest, in both viscous and inviscid environments. We specifically investigate the role of the Reynolds number, as in case A1. Again, we clarify that the cases considered in Tchieu *et al.*<sup>19</sup> have different initial conditions than the viscous simulation for reasons mentioned in Sec. IV A 1. In all cases of this section, the slave initially is placed at a separation distance  $s = D_m/5$  from the master (Fig. 1).

For the test cases  $D_s = D_m$  and  $D_s = D_m/2$ , results are illustrated in Fig. 9. As can be noticed, for all  $Re$  investigated, the slave's qualitative behavior is the same: the aft cylinder is accelerated from rest, it experiences a side force which moves the cylinder into the wake, then drafts in the master's wake, travels a certain distance behind the master and progressively slows down until it stops. In all cases the separation distance in the horizontal direction  $s_x$  is observed to monotonically increase in time. Consistently with case A1, a viscous flow is shown to improve the ability of the master to drag along the slave cylinder. Moreover, in the inviscid case where the slave cylinder is at rest, the same trend occurs. The side force generated in the low pressure region between the two cylinders pulls the slave cylinder behind the master and then the slave stops. As seen in Figs. 9(c) and 9(d), the inviscid case gives the maximum separation and is pulled only very slightly in the positive  $x$ -direction.

As already observed in case A1, a further diameter reduction to  $D_s = D_m/4$ , reveals the existence of two threshold Reynolds numbers, corresponding to transitions to different qualitative behaviors (see Fig. 10). In particular, for  $Re < 30$ , the horizontal separation distance  $s_x$  monotonically increases in time, for  $30 \leq Re \leq 49$  the slave is further accelerated and the separation  $s_x$  nearly drops to zero

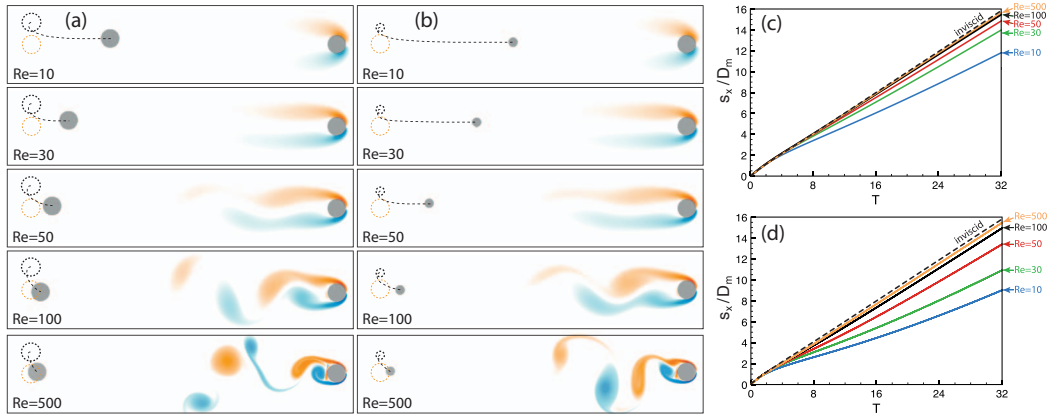


FIG. 9. Case A2. (a) Test case  $D_s = D_m$  at dimensionless time  $T = 32$  for several  $Re$ . Master (initial position is represented by the orange dashed cylinder) and slave (full grey aft cylinder, where the initial position is represented by the black dashed cylinder) are superimposed to the corresponding vorticity field. (b) Test case  $D_s = D_m/2$  at dimensionless time  $T = 32$ : vorticity fields. (c) Normalized separation distance in the horizontal direction  $s_x/D_m$  as function of dimensionless time  $T$  for test case  $D_s = D_m$ . (d) Normalized separation distance in the horizontal direction  $s_x/D_m$  as function of dimensionless time  $T$  for test case  $D_s = D_m/2$ . In (c) and (d) solid (blue, green, red, black, and orange) lines correspond to  $Re = 10, 30, 50, 100$ , and 500 whereas the dashed line corresponds to the inviscid case.

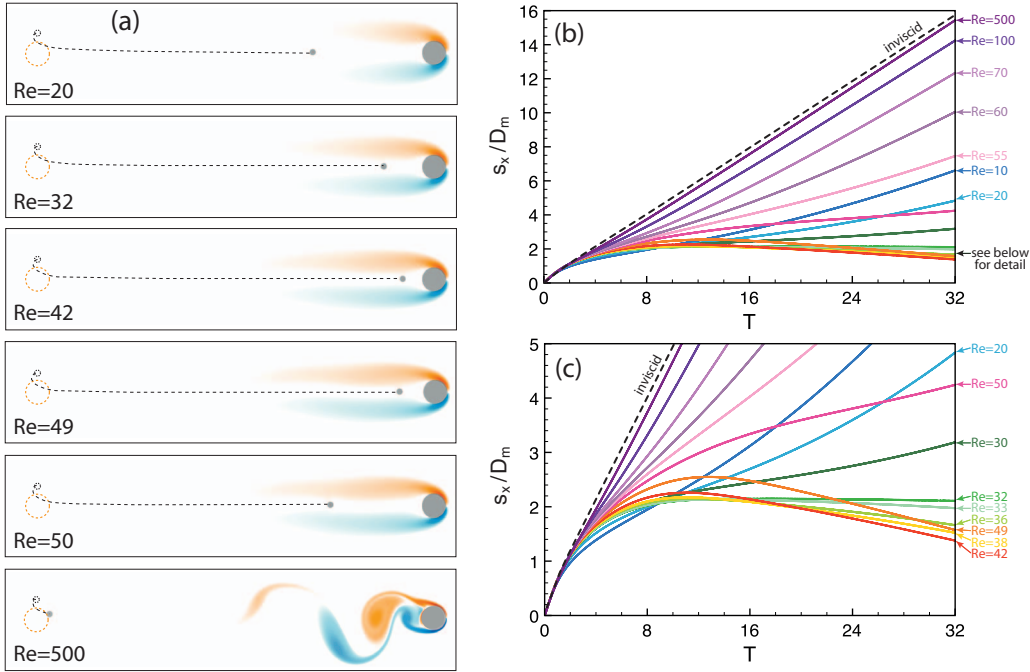


FIG. 10. Case A2. (a) Test case  $D_s = D_m/4$  at dimensionless time  $T = 32$  for several  $Re$ . The master (initial position is represented by the orange dashed cylinder) and slave (full grey aft cylinder, where the initial position is represented by the black dashed cylinder) cylinders are superimposed to the corresponding vorticity field. (b) Normalized separation distance in the horizontal direction  $s_x/D_m$  as function of dimensionless time  $T$ . Solid lines correspond to Reynolds number ranging between 10 and 500. Dashed line corresponds to the inviscid case. (c) Enlargement of panel (b).

and finally for  $Re > 49$ ,  $s_x$  is again observed to increase in time. Varying the initial master-slave distance, we always observed either a monotonically increase of  $s_x$  or sudden accelerations as in the last case. We mention that similar behavior may occur for  $D_s = D_m$  and  $D_s = D_m/2$  for  $Re < 10$ , but we could not investigate such scenarios due to the prohibitive computational costs related to diffusion constraints.

It is concluded that the phenomena illustrated using the method defined in Tchieu *et al.*<sup>19</sup> cannot qualitatively reproduce the effects discovered when the slave cylinder is initially at rest in a viscous environment. More specifically the induced motion in the inviscid case is minimal while viscosity effects increase the fluid-mediated response of the slave cylinder. With increasing viscosity, it appears that bodies smaller than the master cylinder can experience a free ride from rest by sitting in the wake of the master cylinder. This may have interesting implications of viscous transport of material via biogenic ocean mixing as discussed in Katija and Dabiri<sup>43</sup> and Dabiri.<sup>44</sup> At most, the inviscid solutions only provide a lower limit of interaction when the slave body is initially at rest.

As with configuration A1, to assess how the finite size of the slave cylinder affects the fluid-mediated interactions, we plot the paths of passive tracers for  $Re = 50$  and  $500$  in Fig. 11. The passive tracers are initially located at  $y/D_m = 1.2, 0.95, 0.825$  with respect to the master cylinder (corresponding to simulations in case A2 with  $D_s/D_m = 1.0, 0.5, 0.25$ ). The distance traveled is compared in Fig. 12. Note the similarities in path initially taken by both the passive tracer and the respective slave cylinder. The passive tracer and the cylinder both initially travel in the negative  $x$ -direction before going in the positive direction. For  $Re = 50$ , the passive tracers exhibit the same qualitative behavior described in case A1. At  $D_s/D_m = 0.25$  the passive tracer is pulled further to the right than the slave cylinder. At  $D_s/D_m = 0.5$  and  $1$  the slave cylinder moves further downstream than the passive tracer, but the differences are slight. For  $Re = 500$  (Fig. 12(b)), we see that the slave cylinders drift to the right at a higher velocity than the passive tracers as in case A1.

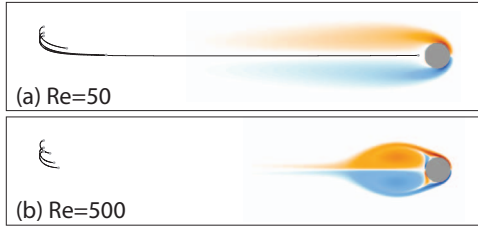


FIG. 11. The advection of a passive tracer up to  $T = 32$  initialized above the forced cylinder for (a)  $Re = 50$  and (b)  $Re = 500$ . The passive tracer is initially placed at a distance  $y/D_m = 1.2, 0.95, 0.825$  corresponding to the center of the slave cylinders for cases  $D_s/D_m = 0.25, 0.5, 0.25$  (dotted line, black, blue, red, respectively) with  $s/D_m = 0.2$ . Grey dots indicate the starting and ending positions of the tracers. Vorticity field is given for reference.

We note that additional simulations where the slave cylinder was placed at oblique angles trailing the master cylinder were performed and no significant differences were observed between these cases and those presented in Sec. IV A, thus these results are omitted for brevity.

### B. Slave's response to master's horizontal oscillation: Case B

In this section, inspired by the work of Nair and Kanso<sup>18</sup> in potential flow (also see Lamb<sup>45</sup> and Borisov *et al.*<sup>46</sup>), we considered the slave's response when the master is forced to oscillate horizontally (Fig. 1, case B). We performed simulations of incompressible, viscous flows in which the master is impulsively started and the slave is initially at rest. All simulations were carried out in the computational domain  $\Sigma = [0, 1] \times [0, 1]$ , in which the master of diameter  $D_m = 0.05$ , initially located at  $(0.4, 0.5)$ , oscillates horizontally according to  $\mathbf{x}_m = A \sin(2\pi t/\mathcal{T} + \phi)$ , where  $\mathbf{x}_m$  is its center of mass and  $A$ ,  $\mathcal{T}$ , and  $\phi$ , respectively, oscillation amplitude, period and phase. In all cases  $ER = 2048 \times 2048$  and  $\mathcal{T} = 1$  physical time unit.

As for case A1 and A2, we focused on the effect of the Reynolds number ( $10 \leq Re \leq 100$ ) on the system's dynamics. Here the characteristic velocity was defined as  $|\mathbf{U}_m| = |2\pi A/\mathcal{T}|$  and therefore  $Re = 2\pi A D_m / (\nu \mathcal{T})$ . Furthermore, the systems investigated were characterized by  $A = D_m$ , initial separation distance  $2D_m \leq d \leq 5D_m$ , initial slave's location  $(0.4 + d, 0.5)$  and diameter  $0.1D_m \leq D_s \leq 1.25D_m$ .

In Fig. 13(a), we report the slave's normalized displacement ( $\Delta x/D_m$ , positive and negative  $\Delta x$ , correspond, respectively, to repulsion and attraction by the master), versus the dimensionless time  $T = 4\pi At / (\mathcal{T} D_m)$ , for the system characterized by  $D_s = D_m$ ,  $d = 2.5D_m$  and  $\phi = 0$ . Similar to cases A1 and A2, we observe a change in qualitative behavior as a function of the Reynolds number. In fact, when  $Re > 27$ , the slave is repelled by the master as observed in Fig. 13(c), while for

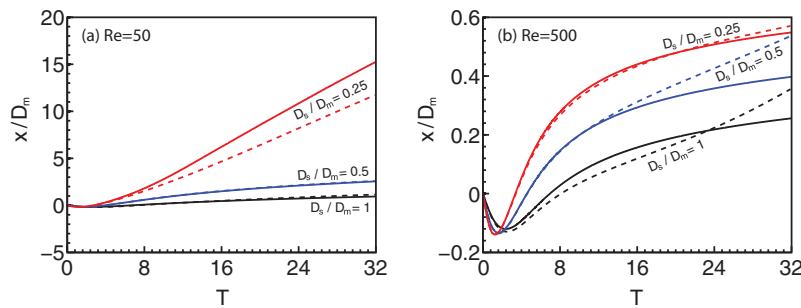


FIG. 12. The distance traveled to the right by a slave cylinder of diameter  $D_s/D_m = 0.25, 0.5, 0.25$  (dotted line, black, blue, red, respectively) with  $s/D_m = 0.2$  and a passive tracer (solid line) initially located at the position corresponding to the center of the slave cylinder for (a)  $Re = 50$  and (b)  $Re = 500$ . The passive tracer is initially placed at a distance  $y/D_m = 1.2, 0.95, 0.825$  (black, blue, red) with respect to the center of the master cylinder. Note that oscillatory vortex shedding is not visible in (b) as compared to Fig. 11 because the flow remains symmetric.

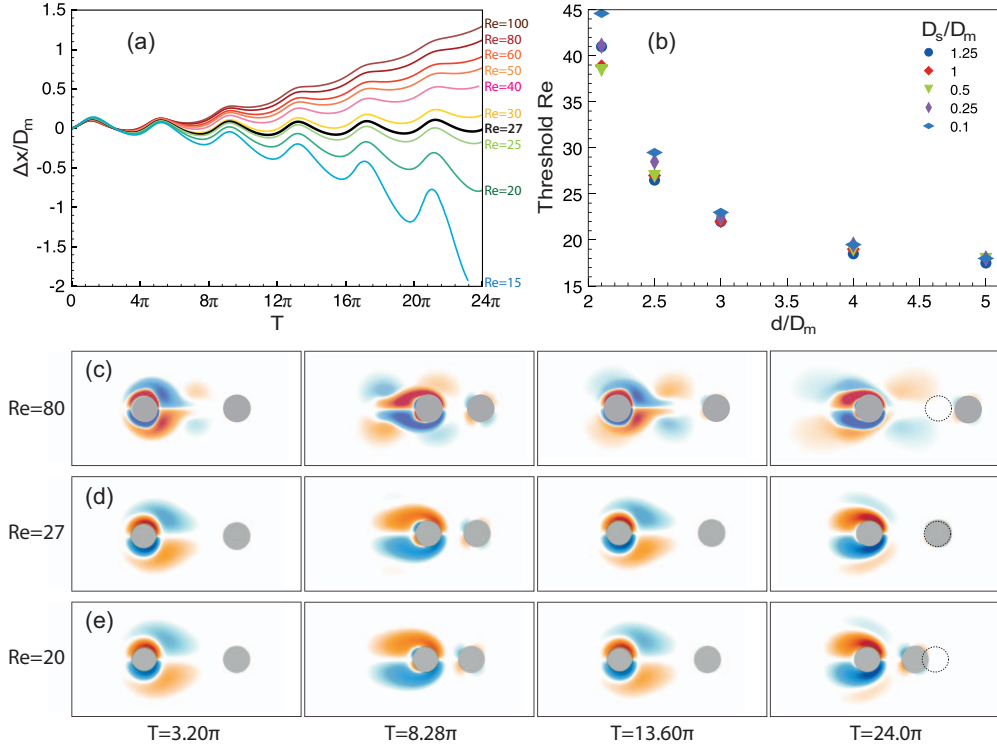


FIG. 13. Case B. (a) Slave's normalized displacement ( $\Delta x/D_m$ ) versus dimensionless time  $T$ , for several Reynolds numbers (from top to bottom  $Re = 100, 80, 60, 50, 40, 30, 27, 25, 20, 15$ ) and  $\phi = 0$ ,  $A = D_m$ ,  $D_s = D_m$ ,  $d = 2.5D_m$ . (b) Threshold Reynolds number ( $Re_{th}$ ) as function of  $D_s/D_m$  and  $d/D_m$ . (c)–(e) Evolution in time of the vorticity fields for the cases  $Re = 80, 27$ , and  $20$  reported in panel (a). The dashed cylinder represents the initial slave's location.

$Re < 27$ , the slave is attracted as observed in Fig. 13(e). The threshold value of  $Re_{th} \simeq 27$ , corresponds to the slave oscillating around its initial position (Fig. 13(d)). The vorticity plots, Figs. 13(c)–13(e), reveal that for  $Re > 27$ , the flow develops a secondary structure constituted by a top and bottom patch of, respectively, positive and negative vorticity. Such structure, inducing a flow to the right of the master, contributes to the repulsion of the slave. On the other hand, an increase in viscosity, is responsible for a quick dissipation of this structure, favoring the attraction of the slave by the master.

As mentioned above, the same study was carried out for several configurations where both  $d/D_m$  and  $D_s/D_m$  were varied, in order to assess the impact of these parameters on the system. All simulations presented the same trend as the one above described and the threshold Reynolds

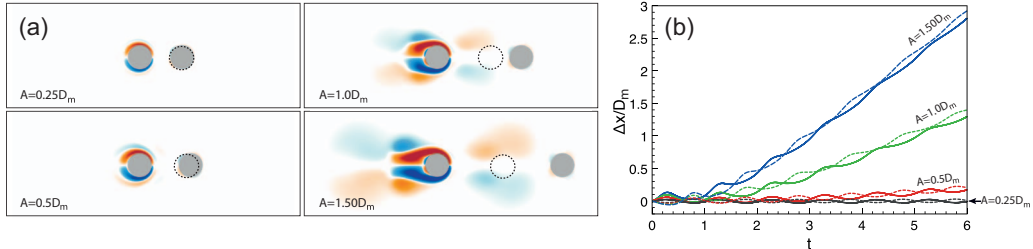


FIG. 14. Case B. Vorticity fields at physical time  $t = 6$ , corresponding to oscillation amplitudes  $A = 1.5D_m$ ,  $A = 1D_m$ ,  $A = 0.5D_m$ ,  $A = 0.25D_m$ , and  $\phi = 0$ . The dashed cylinder represents the initial slave's location. (b) Slave's normalized displacement ( $\Delta x/D_m$ ) versus physical time  $t$  for  $A = 1.5D_m$  (blue),  $A = 1D_m$  (green),  $A = 0.5D_m$  (red),  $A = 0.25D_m$  (black). Solid and dashed lines correspond, respectively, to  $\phi = 0$  and  $\phi = \pi$ .

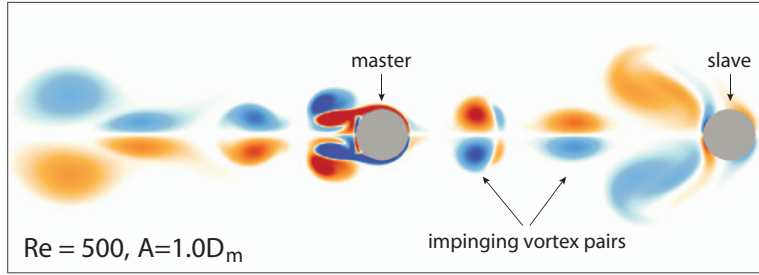


FIG. 15. Vorticity field at physical time  $t = 6$ , with oscillation amplitude  $A = D_m$ ,  $Re = 500$ , and  $\phi = 0$ . The slave cylinder on the right is free to move. Shades are over saturated to clearly show how the vortex pair created from the motion of the master cylinder impinges on the slave cylinder, imparting it with positive  $x$ -momentum.

numbers identified, given the pairs  $(d/D_m - D_s/D_m)$  are reported in Fig. 13(b). The initial separation distance  $d/D_m$  strongly influences  $Re_{th}$  causing its exponential decay. On the other hand, the diameter ratio  $D_s/D_m$ , does not substantially affect  $Re_{th}$ , revealing that the flow features play a more important role than the inertia of the slave.

We note that in the study of Nair and Kanso,<sup>18</sup> a change in the system's qualitative behavior was achieved by switching the oscillation phase from  $\phi = \pi$  (repulsion) to  $\phi = 0$  (attraction). In a viscous environment this behavior is not observed and to an out-of-phase oscillation simply corresponds an out-of-phase slave's displacement curve, without causing any change in qualitative behavior, whether repulsive or attractive. For clarity we did not report out-of-phase curves in Fig. 13(a), nevertheless, as an example, slave's displacement curves are depicted in Fig. 14(b) for  $Re = 100$ . In such simulations the oscillation amplitude was set between  $0.25D_m \leq A \leq 1.5D_m$  and the slave was initialized at  $(0.4 + 1.5D_m + A, 0.5)$ . As can be noticed the larger the amplitude  $A$ , the stronger the repulsion of the slave from the master, but switching phase did not affect the slave's drifting direction. It is observed, even initially in the first period, that the viscous and inviscid case are qualitatively different. For example, in the inviscid case, for sinusoidal forcing with  $\phi = 0$  ( $\phi = \pi$ ), it has been shown that the slave cylinder is initially attracted to (repelled by) the master cylinder.<sup>18</sup> In all viscous cases, both the master and slave cylinder oscillate in phase. In a more global sense, the long time behavior is also different. In inviscid cases where  $\phi = 0$ , the slave cylinder is initially attracted and then repelled given large initial separation distances or attracted to the point of collision with the master cylinder for shorter initial separation distances.<sup>18,46</sup> In viscous simulations, the creation of a vortex dipole (see Fig. 15) that impinges on the slave cylinder at every cycle transports momentum from the fluid to the slave cylinder allowing it to more effectively move away from the oscillating cylinder. This mechanism is not present when  $Re < 27$  where the dipoles are less intense and drastically diffuse before reaching the slave cylinder. The transfer of momentum is exacerbated by both the increase in oscillation amplitude and Reynolds number where the transport momentum becomes more highly correlated with the imposed  $x$ -motion of the master cylinder. We show a simulation at  $Re = 500$  to demonstrate the creation of successive dipoles and the subsequent impingement on the slave cylinder (Fig. 15).

We note that passive tracers were also introduced in the flow for comparison. The paths of the tracers were found to be qualitatively the same as the slave cylinder, e.g., attracted to the cylinder when  $Re = 20$  and repelled when  $Re = 80$ .

## V. CONCLUSIONS

We considered the dynamics of two interacting moving cylinders immersed in a two-dimensional viscous, incompressible flow. The simulations are performed via a wavelet adapted, multi resolution, remeshed vortex method coupled with Brinkman penalization and projection approach. The present viscous studies have been motivated by related potential flow simulations of slave-master cylinder interactions<sup>18,19</sup> and are aimed to assess the role of finite Reynolds numbers in these situations.

The method is validated on the problem of two interacting cylinders, computing the forces experienced by both solids. Results were found to be in good agreement with reference simulations and an error analysis of the method is presented to assess its convergence in space and time.

Two flow mediated problems were considered, involving a master cylinder forced to move forward (cases A1 and A2) and to oscillate horizontally (case B) and a slave cylinder free to respond. In both cases the qualitative response of the system was found to depend on the Reynolds number, responsible for sharp transitions between different regimes. In case A1 and A2, the Reynolds number is responsible for sudden accelerations of the slave, while, in case B, it dictates whether the slave is repelled or attracted by the master. In some instances of cases A1 and A2, it is even possible that the slave cylinder is pulled further downstream by the master cylinder than if the slave cylinder were replaced by a passive particle. Thus, in specific cases, a finite size particle may be transported more effectively through fluid-mediated interactions than even passive tracers.

We conclude by demonstrating that there can be drastic differences in the behavior of interacting bodies as simulated by potential flow simulations and by viscous simulations at finite and moderate Reynolds numbers. It is worth mentioning that at these moderate Reynolds numbers, three-dimensional instabilities may occur (e.g., for the circular cylinder, the onset of instability occurs at  $Re \approx 200$ , see Ref. 47). Simulations in three dimensions are, at the moment, prohibitively costly (the added dimensionality makes simulations orders of magnitude more expensive) and thus we have presented a two-dimensional analog here in hopes of elucidating fundamental Reynolds number effects on the fluid-mediated interactions. Future work will focus on extending the Reynolds number regime of the present studies and adding capabilities to simulate self-propelled, three-dimensional swimmers.

## ACKNOWLEDGMENTS

We wish to thank Manfred Quack and Diego Rossinelli for their support on MRAG and Babak Hejazialhosseini for his deep discussions.

- <sup>1</sup>D. Weihs, "Hydromechanics of fish schooling," *Nature (London)* **241**(5387), 290–291 (1973).
- <sup>2</sup>J. C. Liao, D. N. Beal, G. V. Lauder, and M. S. Triantafyllou, "Fish exploiting vortices decrease muscle activity," *Science* **302**(5650), 1566–1569 (2003).
- <sup>3</sup>D. Weihs, "The hydrodynamics of dolphin drafting," *J. Biol.* **3**(2), 8 (2004), see online at <http://jbiol.com/content/3/2/8>.
- <sup>4</sup>V. Gyrya, I. S. Aranson, L. V. Berlyand, and D. Karpeev, "A model of hydrodynamic interaction between swimming bacteria," *Bull. Math. Biol.* **72**(1), 148–183 (2010).
- <sup>5</sup>T. Ishikawa, M. P. Simmonds, and T. J. Pedley, "Hydrodynamic interaction of two swimming model micro-organisms," *J. Fluid Mech.* **568**, 119–160 (2006).
- <sup>6</sup>D. L. Koch and G. Subramanian, "Collective hydrodynamics of swimming microorganisms: Living fluids," *Annu. Rev. Fluid Mech.* **43**, 637–659 (2011).
- <sup>7</sup>B. Metzger, M. Nicolas, and E. Guazzelli, "Falling clouds of particles in viscous fluids," *J. Fluid Mech.* **580**, 283–301 (2007).
- <sup>8</sup>M. Nicolas, "Experimental study of gravity-driven dense suspension jets," *Phys. Fluids* **14**(10), 3570–3576 (2002).
- <sup>9</sup>G. A. Voth, B. Bigger, M. R. Buckley, W. Losert, M. P. Brenner, H. A. Stone, and J. P. Gollub, "Ordered clusters and dynamical states of particles in a vibrated fluid," *Phys. Rev. Lett.* **88**(23), 234301 (2002).
- <sup>10</sup>N. Bampalis and J. M. R. Graham, "Flow-induced forces arising during the impact of two circular cylinders," *J. Fluid Mech.* **616**, 205–234 (2008).
- <sup>11</sup>J. A. Riffell and R. K. Zimmer, "Sex and flow: the consequences of fluid shear for sperm-egg interactions," *J. Exp. Biol.* **210**(20), 3644–3660 (2007).
- <sup>12</sup>B. Basso, J. Love, and J. K. Hedrick, "Airborne, autonomous and collaborative," *Mech. Eng. (Am. Soc. Mech. Eng.)* **133**(4), 26–32 (2011).
- <sup>13</sup>H. Park, F. Noca, and P. Koumoutsakos, "Vortobots: vortex-generating microscopic robots would move in swarms," NASA Tech Briefs, Control No. NP0-21188, NASA's Jet Propulsion Laboratory, 2005.
- <sup>14</sup>J. F. Brady and G. Bossis, "Stokesian dynamics," *Annu. Rev. Fluid Mech.* **20**, 111–157 (1988).
- <sup>15</sup>S. T. Kim, Y. O. Fuentes, and S. J. Karrila, "Towards as initio simulations of concentrated suspensions," *J. Stat. Phys.* **62**(5-6), 1197–1223 (1991).
- <sup>16</sup>M. Sebastian and E. Lauga, "The long-time dynamics of two hydrodynamically-coupled swimming cells," *Bull. Math. Biol.* **72**(4), 973–1005 (2010).
- <sup>17</sup>G. Subramanian and D. L. Koch, "Evolution of clusters of sedimenting low-Reynolds-number particles with Oseen interactions," *J. Fluid Mech.* **603**, 63–100 (2008).
- <sup>18</sup>S. Nair and E. Kanso, "Hydrodynamically coupled rigid bodies," *J. Fluid Mech.* **592**, 393–411 (2007).
- <sup>19</sup>A. A. Tchieu, D. Crowdy, and A. Leonard, "Fluid-structure interaction of two bodies in an inviscid fluid," *Phys. Fluids* **22**(10), 107101 (2010).

- <sup>20</sup>R. Glowinski, T. W. Pan, T. I. Hesla, D. D. Joseph, and J. Periaux, "A fictitious domain approach to the direct numerical simulation of incompressible viscous flow past moving rigid bodies: Application to particulate flow," *J. Comput. Phys.* **169**(2), 363–426 (2001).
- <sup>21</sup>M. Gazzola, P. Chatelain, W. M. van Rees, and P. Koumoutsakos, "Simulations of single and multiple swimmers with non-divergence free deforming geometries," *J. Comput. Phys.* **230**(19), 7093–7114 (2011), see online at <http://www.sciencedirect.com/science/article/pii/S0021999111002737>.
- <sup>22</sup>J. Eldredge, "A reconciliation of viscous and inviscid approaches to computing locomotion of deforming bodies," *Exp. Mech.* **50**, 1349–1353 (2010).
- <sup>23</sup>H. Fukuda, S. Torisawa, Y. Sawada, and T. Takagi, "Ontogenetic changes in schooling behaviour during larval and early juvenile stages of pacific bluefin tuna thunnus orientalis," *J. Fish Biol.* **76**(7), 1841–1847 (2010).
- <sup>24</sup>M. E. Huntley and M. Zhou, "Influence of animals on turbulence in the sea," *Mar. Ecol.: Prog. Ser.* **273**, 65–79 (2004).
- <sup>25</sup>P. Koumoutsakos and A. Leonard, "High-resolution simulations of the flow around an impulsively started cylinder using vortex methods," *J. Fluid Mech.* **296**, 1–38 (1995).
- <sup>26</sup>G. H. Cottet and P. Poncet, "Advances in direct numerical simulations of 3d wall-bounded flows by vortex-in-cell methods," *J. Comput. Phys.* **193**(1), 136–158 (2004).
- <sup>27</sup>M. Bergdorf and P. Koumoutsakos, "A lagrangian particle-wavelet method," *Multiscale Model. Simul.* **5**(3), 980–995 (2006).
- <sup>28</sup>O. V. Vasilyev and N. K. R. Kevlahan, "Hybrid wavelet collocation-Brinkman penalization method for complex geometry flows," *Int. J. Numer. Methods Fluids* **40**(3-4), 531–538 (2002).
- <sup>29</sup>M. Coquerelle and G. H. Cottet, "A vortex level set method for the two-way coupling of an incompressible fluid with colliding rigid bodies," *J. Comput. Phys.* **227**(21), 9121–9137 (2008).
- <sup>30</sup>B. Hejazialhosseini, D. Rossinelli, M. Bergdorf, and P. Koumoutsakos, "High order finite volume methods on wavelet-adapted grids with local time-stepping on multicore architectures for the simulation of shock-bubble interactions," *J. Comput. Phys.* **229**(22), 8364–8383 (2010).
- <sup>31</sup>D. Rossinelli, B. Hejazialhosseini, M. Bergdorf, and P. Koumoutsakos, "Wavelet-adaptive solvers on multi-core architectures for the simulation of complex systems," *Concurrency Comput.: Pract. Exper.* **23**(2), 172–186 (2011).
- <sup>32</sup>D. Rossinelli, B. Hejazialhosseini, D. G. Spampinato, and P. Koumoutsakos, "Multicore/multi-gpu accelerated simulations of multiphase compressible flows using wavelet adapted grids," *SIAM J. Sci. Comput. (USA)* **33**(2), 512–540 (2011).
- <sup>33</sup>P. Ploumhans and G. S. Winckelmans, "Vortex methods for high-resolution simulations of viscous flow past bluff bodies of general geometry," *J. Comput. Phys.* **165**(2), 354–406 (2000).
- <sup>34</sup>G. H. Cottet and P. Koumoutsakos, *Vortex Methods, Theory and Practice* (Cambridge University Press, Cambridge, England, 2000).
- <sup>35</sup>E. Arquis and J. P. Caltagirone, "On the hydrodynamical boundary-conditions along a fluid layer porous-medium interface - application to the case of free convection," *C. R. Acad. Sci., Ser. II: Mec., Phys., Chim., Sci. Terre Univers* **299**(1), 1–4 (1984).
- <sup>36</sup>P. Angot, C. H. Bruneau, and P. Fabrie, "A penalization method to take into account obstacles in incompressible viscous flows," *Numer. Math.* **81**(4), 497–520 (1999).
- <sup>37</sup>D. Rossinelli, M. Bergdorf, G. H. Cottet, and P. Koumoutsakos, "Gpu accelerated simulations of bluff body flows using vortex particle methods," *J. Comput. Phys.* **229**(9), 3316–3333 (2010), see online at <http://www.sciencedirect.com/science/article/B6WHY-4Y6J428-2/2/0ddb10a20cfce335ebaf14d221dabc46>.
- <sup>38</sup>N. A. Patankar and N. Sharma, "A fast projection scheme for the direct numerical simulation of rigid particulate flows," *Commun. Numer. Methods Eng.* **21**(8), 419–432 (2005).
- <sup>39</sup>J. Barnes and P. Hut, "A hierarchical o(n-log-n) force-calculation algorithm," *Nature (London)* **324**(6096), 446–449 (1986).
- <sup>40</sup>L. Greengard and V. Rokhlin, "A fast algorithm for particle simulations," *J. Comput. Phys.* **73**(2), 325–348 (1987).
- <sup>41</sup>D. Rossinelli, "Multiresolution flow simulations on multi/many-core architectures," Ph.D. dissertation (ETH Zurich, 2011).
- <sup>42</sup>P. Koumoutsakos, "Multiscale flow simulations using particles," *Annu. Rev. Fluid Mech.* **37**, 457–487 (2005).
- <sup>43</sup>K. Katija and J. O. Dabiri, "A viscosity-enhanced mechanism for biogenic ocean mixing," *Nature (London)* **460**(7255), 624–627 (2009).
- <sup>44</sup>John O. Dabiri, "Role of vertical migration in biogenic ocean mixing," *Geophys. Res. Lett.* **37**, L11602, doi:10.1029/2010GL043556 (2010).
- <sup>45</sup>H. Lamb, *Hydrodynamics* (Dover, New York, 1945).
- <sup>46</sup>A. V. Borisov, I. S. Mamaev, and S. M. Ramodanov, "Dynamics of two interacting circular cylinders in perfect fluid," *Discrete Contin. Dyn. Syst.* **19**(2), 235–253 (2007).
- <sup>47</sup>C. H. Williamson, "Three-dimensional wake transition," *J. Fluid Mech.* **328**, 345–407 (1996).